

## Full length article

## Time, stress, and temperature-dependent deformation in nanostructured copper: Stress relaxation tests and simulations



Xu-Sheng Yang<sup>a,1</sup>, Yun-Jiang Wang<sup>b,1</sup>, Guo-Yong Wang<sup>c</sup>, Hui-Ru Zhai<sup>a</sup>, L.H. Dai<sup>b</sup>,  
Tong-Yi Zhang<sup>d,\*</sup>

<sup>a</sup> Department of Mechanical and Aerospace Engineering, The Hong Kong University of Science and Technology, Clear Water Bay, Kowloon, Hong Kong, China

<sup>b</sup> State Key Laboratory of Nonlinear Mechanics, Institute of Mechanics, Chinese Academy of Sciences, Beijing 100190, China

<sup>c</sup> Key Laboratory of Automobile Materials, Department of Materials Science and Engineering, Jilin University, No. 5988 Renmin Street, Changchun 130025, China

<sup>d</sup> Shanghai University Materials Genome Institute and Shanghai Materials Genome Institute, Shanghai University, 99 Shangda Road, Shanghai 200444, China

## ARTICLE INFO

## Article history:

Received 30 October 2015

Received in revised form

5 February 2016

Accepted 9 February 2016

## Keywords:

Stress relaxation

Nanotwin

Copper

HRTEM

Atomistic simulations

## ABSTRACT

In the present work, stress relaxation tests, high-resolution transmission electron microscopy (HRTEM), and molecular dynamics (MD) simulations were conducted on coarse-grained (cg), nanograined (ng), and nanotwinned (nt) copper at temperatures of 22 °C (RT), 30 °C, 40 °C, 50 °C, and 75 °C. The comprehensive investigations provide sufficient information for the building-up of a formula to describe the time, stress, and temperature-dependent deformation and clarify the relationship among the strain rate sensitivity parameter, stress exponent, and activation volume. The typically experimental curves of logarithmic plastic strain rate versus stress exhibited a three staged relaxation process from a linear high stress relaxation region to a subsequent nonlinear stress relaxation region and finally to a linear low stress relaxation region, which only showed-up at the test temperatures higher than 22 °C, 22 °C, and 30 °C, respectively, in the tested cg-, ng-, and nt-Cu specimens. The values of stress exponent, stress-independent activation energy, and activation volume were determined from the experimental data in the two linear regions. The determined activation parameters, HRTEM images, and MD simulations consistently suggest that dislocation-mediated plastic deformation is predominant in all tested cg-, ng-, and nt-Cu specimens in the initial linear high stress relaxation region at the five relaxation temperatures, whereas in the linear low stress relaxation region, the grain boundary (GB) diffusion-associated deformation is dominant in the ng- and cg-Cu specimens, while twin boundary (TB) migration, i.e., twinning and detwinning with parallel partial dislocations, governs the time, stress, and temperature-dependent deformation in the nt-Cu specimens.

© 2016 Acta Materialia Inc. Published by Elsevier Ltd. All rights reserved.

## 1. Introduction

Creep and stress relaxation behaviors of metallic materials are extremely important to their applications in industries. The behaviors depend highly on time, stress, and temperature and are the responses of microstructures of metallic materials to external loading conditions of time, stress, and temperature. Plastic deformation in polycrystalline metals can be mediated by dislocation activities, grain boundary (GB) and twin boundary (TB) movement,

and GB diffusion. GBs are strong obstacles against dislocation movement, and therefore refining grain size is an important approach to strengthen metallic materials as indicated by the famous Hall–Petch relation [1,2]. Too many strong dislocation-motion obstacles of GBs might lead to the brittleness in nanograined (ng) metals. The TB resistance against dislocation motion is much more moderated, especially in face-centered cubic (fcc) metals, thereby simultaneously strengthening and toughening nanotwinned (nt) metals [3–8]. When the grain size is small, however, GB diffusion or Coble creep [9–11], GB sliding [12–14], grain rotation [15], etc., might become the predominant modes of the time-dependent deformation [16–18]. In general, the GB-diffusional deformation and the dislocation-mediated deformation are respectively dominant at low and high strain rates/stresses

\* Corresponding author.

E-mail address: [zhangty@shu.edu.cn](mailto:zhangty@shu.edu.cn) (T.-Y. Zhang).

<sup>1</sup> These authors contributed equally to this work.

[14]. Since coherent TBs are not fast diffusion channels [19–21], the nominal dislocation-mediated plasticity might switch to the twinning and detwinning mechanism in nt-Cu, leading to the change from normal Hall–Petch relation to revised Hall–Petch relation [22].

Deformation activation energy and activation volume might reflect the mechanism of thermally activated plastic deformation [23–26]. The activation volume represents the generalized change in volume caused by flow stress and the generalized area swept over by mobile dislocations in dislocation mediated plasticity. Deformation activation energy and activation volume can be determined by stress relaxation tests at various temperatures. For example, the data of stress relaxation tests on Al–Zn–Mg–Cu alloy at temperatures of 120 °C, 160 °C, and 200 °C [27] were illustrated in curves of logarithmic strain rate versus logarithmic stress, showing (i) initial high stress stage, (ii) middle stress transition stage, and (iii) last low stress stage. The obtained activation energy and the stress exponent suggested that dislocation creep was the dominant deformation mechanism in the initial high-stress and subsequent medium-stress stages; whereas diffusional creep was the mechanism in the last low-stress stage. Although repeated stress relaxation tests and strain rate jump tests were conducted over temperatures (77–373 K) on the electrodeposited (ED) ng-Ni with an average grain size of about 30 nm [28], the apparent activation volume and the physical activation volume were determined only at a given temperature [29], thereby giving temperature-dependent values. The difference in the time, stress, and temperature-dependent deformation behavior between the ng-Ni and the coarse-grained (cg) Ni counterpart might indicate that the thermally activated process in ng-Ni was controlled by the GB-mediated dislocation process. The seven-hours-long stress relaxation tests on ng-Ni with an average grain size of 27 nm at room temperature (RT) [16,17] determined the activation volume, which values were over  $23 b^3$ , about  $15 b^3$ , and around  $1.7 b^3$  in the near linear rapidly stress delayed, lumber nonlinear stress delayed, and near linear slowly stress delayed regions, respectively, where  $b$  denotes the magnitude of Burgers vector. The change in the activation volume implied the deformation transition from the initial dislocation-dominated plasticity to the mixture of dislocation motion and diffusion-based GB activity and finally to the entire diffusion-based GB activity. The stress relaxation tests [30] on ED ng-Ni with grain size of 21 nm and high pressure torsion (HPT) produced ng-Ni with grain size of 105 nm at RT showed a decreased activation volume with increasing stress in the ED ng-Ni and an opposite trend in the HPT ng-Ni. The indentation stress relaxation tests [31] on the rolled and annealed ng-Ni with an average grain size of 20 nm at RT showed that the activation volume in the rolled ng-Ni was decreased first and then increased as the rolling strain increasing, and the activation volume in the annealed Ni was continuously increased with the increase of annealing temperature. Stress relaxation tests on nt-Cu with twin lamellae thicknesses of 35 and 15 nm at RT [32] indicated that the apparent activation volume and the physical activation volume were about  $20 b^3$  and  $15.5 b^3$ ,  $36 b^3$  and  $30 b^3$ , and  $350 b^3$  and  $309 b^3$  for the nt-15, nt-35, and cg specimens, respectively, which were correspondingly attributed to the TB-mediated plasticity and the intra-twin dislocation activity.

The above description indicates that the apparent activation energy depends on the stress level. To experimentally determine the apparent activation energy, one must have the experiment data of the plastic deformation rate under a certain stress level at various temperatures. Then, the activation volume can be extracted from the stress-dependent apparent activation energy. Clearly, to acquire more information about the time, stress, and temperature-dependent deformation, stress relaxation tests must be conducted at various temperatures. In the present work, stress relaxation tests

were conducted on cg, ng, and nt copper at temperatures of RT (–22 °C), 30 °C, 40 °C, 50 °C, and 75 °C to investigate the time, stress, and temperature-dependent deformation. We clarify the relationship between the strain rate sensitivity parameter, stress exponent, and activation volume. Together with the evidence from the high-resolution transmission electron microscopy (HRTEM) and molecular dynamics (MD) simulations, we suggest the predominant deformation mechanisms under different stress levels in the cg, ng, and nt-Cu specimens.

This paper is organized as follows. Section 2 gives the experimental methods that include the synthesis methods of the used copper specimens with different microstructures, the procedure of stress relaxation tests, and the simulation methodology. Section 3 summarizes experimental and simulation results of stress relaxation, from which the activation parameters in the different stress levels are determined. The results suggest a theoretical formula to describe the time, stress, and temperature-dependent deformation. The relationship between the strain rate sensitivity parameter, stress exponent, and activation volume is also discussed in Section 3. Based on the determined activation parameters, and the evidences from the HRTEM and MD simulation observations, Section 4 mainly discusses the transition in the deformation mechanism from the high stress level to low stress level in the three types of specimens. Finally, concluding remarks are given in Section 5.

## 2. Methods

Commercial pure Cu sheet of ~3 mm thickness was annealed at 400 °C for 4 h to get a cg microstructure. High-pure ng and nt-Cu sheets with dimensions of about 12 cm × 6 cm × 500 μm were synthesized with CuSO<sub>4</sub> electrolyte [33,34]. The density of the synthesized sheets was determined by the Archimedes principle to be  $8.92 \pm 0.02$  g/cm<sup>3</sup>. Dog-bone shaped tensile specimens of with 33 mm overall length, 8 mm gage length and 2.5 mm gage width were cut by an electro-discharge machine from the synthesized sheets. Double surfaces of specimens were polished with SiC papers of 400–1200 grits and alumina suspensions of 0.1 μm, and the final thickness of specimens is ~300 μm. The micro/nanostructure of the cg, ng and nt-Cu before and after tests was characterized by using an optical microscope (OM, Olympus BH2-MJLT) and a transmission electron microscope (TEM, JEOL 2010F) operated at 200 kV.

Stress-relaxation tests were carried out on a Universal Testing Machine (UTM) with Furnace (MTS SINTECH 10/D) at RT, 30 °C, 40 °C, 50 °C, and 75 °C with accuracy  $\pm 1$  °C in air. After the specimens were stretched at the strain loading rate of  $10^{-2}$  s<sup>-1</sup> to a designed stress level, which was 115 MPa for the cg-Cu, 350 MPa for the ng-Cu, and 550 MPa for the nt-Cu, the cross-head was stopped there to allow stress relaxation under sustained strain for 300 s and the stress decay was recorded as a function of time. Then, the relaxed specimen was reloaded to the same stress level with the strain rate  $10^{-1}$  s<sup>-1</sup> to conduct the second cycle of relaxation test. In total, four cycles of repeated stress relaxation tests were carried out on each specimen with the same procedure.

Atomistic simulations were performed with the Large-scale Atomic/Molecular Massively Parallel Simulator (LAMMPS) code [35] and an embedded-atom method (EAM) potential for Cu atoms [36]. The twin-free ng-Cu sample contained 27 randomly orientated Voronoi grains with averaged grain size about 10 nm. The nt-Cu sample was constructed by inserting nts into the ngs and the nt thickness was 1.25 nm on average. The twin plane orientations in the nt sample were also randomly arranged on {111} planes. Each of the ng and nt-Cu, as shown in Fig. 7 (a, e), contained approximately 2,200,000 atoms, with dimensions of about  $30 \times 30 \times 30$  nm<sup>3</sup>. Following the setting-up of the simulated sample, energy minimization was performed at a designed temperature by

using the conjugate gradient algorithm and then thermally equilibrated for 200 ps at the temperature. To mimic the stress relaxation tests, uniaxial tensile loading was first conducted on the simulated sample with a nominal constant strain rate of  $10^8 \text{ s}^{-1}$  until to the nominal strain of 10%. Then, isothermal stress relaxation, with Nosé-Hoover thermostat [37,38], was simulated under the sustained 10% strain for 4 ns. The stress tensor was controlled by a Parrinello-Rahman technique [39] within a  $NPT$  ensemble, where  $N$ ,  $P$ ,  $T$  denotes number of atoms, pressure, and temperature, respectively. The MD time step was 2 fs and the periodic boundary conditions were applied on all directions. The defective atoms were recognized according to common neighbor analysis (CNA), and visualized by OVITO [40].

### 3. Results

#### 3.1. Stress relaxation experimental results

As an example, Fig. 1(a–c) are the OM image of the cg-Cu and the TEM images of the ng, and nt-Cu, respectively, showing that there are very few twins in the ng-Cu, while some annealing microtwins appear in the cg-Cu and many intragranular nanotwins are there in the nt-Cu. The averaged grain size is about  $40 \mu\text{m}$  in the cg-Cu. The  $\{111\}_{fcc}$  TBs of nanotwins are perfectly coherent and atomically sharp, as demonstrated in Fig. 1(d), and no visible defects are observed inside the nanotwins. The intragranular nanotwins divide the ultrafine grains in the nt-Cu into subgrains. The grain size distribution, the subgrain distribution, and the twin lamellar thickness distribution are carefully counted over a  $10 \mu\text{m} \times 10 \mu\text{m}$  area and plotted in Fig. 1(e–g), respectively. The grain size for most grains in the ng-Cu ranges from 20 nm to  $\sim 150$  nm with the highest percentages of grain size around 60–70 nm and a mean grain size is about 70 nm Fig. 1(f) gives the subgrain size distribution in the nt-Cu, which is very much similar

to the grain size distribution in the ng-Cu except that the mean subgrain size is down to 65 nm. The twin lamellar thickness distribution in the nt-Cu is illustrated in Fig. 1(g), indicating that the mean nt thickness is around 50 nm and most twin lamellas have the thicknesses from 20 nm to 80 nm.

Fig. 2(a–c) show the stress as a function of time in the four cycles of stress relaxation tests on the cg, ng, and nt-Cu, respectively, at temperatures of RT, 30 °C, 40 °C, 50 °C, and 75 °C, meanwhile the stress-strain tensile at RT and corresponding relaxation curves are plotted in the Fig. S1(a–d) in the Supplementary material. For a given specimen at a certain relaxation cycle, the magnitude of the total stress drop for the 300 s relaxation period increases with the increase of the test temperature, while for a given specimen at a fixed temperature, the magnitude of the total stress drop decreases with the increase of the relaxation cycle. In comparison with the cg and ng-Cu, the nt-Cu exhibits the most significant stress drop at the same temperature and the same relaxation cycle. For example, Fig. 2(d) shows the stress drop versus relaxation time during the first cycle relaxation at RT, where the stress drop  $\Delta\sigma^t = \sigma(t) - \sigma_0$  and  $\sigma_0$  denotes the relaxation starting stress. The total stress drop  $\Delta\sigma^t$  during the first relaxation cycle at RT is 87 MPa for the nt-Cu, 45 MPa for the ng-Cu and only 15 MPa for the cg-Cu.

The stress relaxation test was performed at a constant strain, which is divided into elastic and plastic strains. Thus, we have

$$\dot{\epsilon} = \dot{\sigma}/M + \dot{\epsilon}_p = 0 \text{ or } \dot{\epsilon}_p = -\dot{\sigma}/M \quad (1)$$

where  $\dot{\epsilon} = d\epsilon/dt$ ,  $\dot{\epsilon}_p = d\epsilon_p/dt$ , and  $\dot{\sigma} = d\sigma/dt$  represent the total strain rate, plastic strain rate, and stress rate, respectively, with  $t$  being the relaxation time; and  $M$  is the nominal elastic modulus of the specimen including the machine influence. The value of  $M$  is determined from Fig. S1(a) to be 124 GPa at RT.

Fig. 3(a–c) show the logarithmic plastic strain rate versus

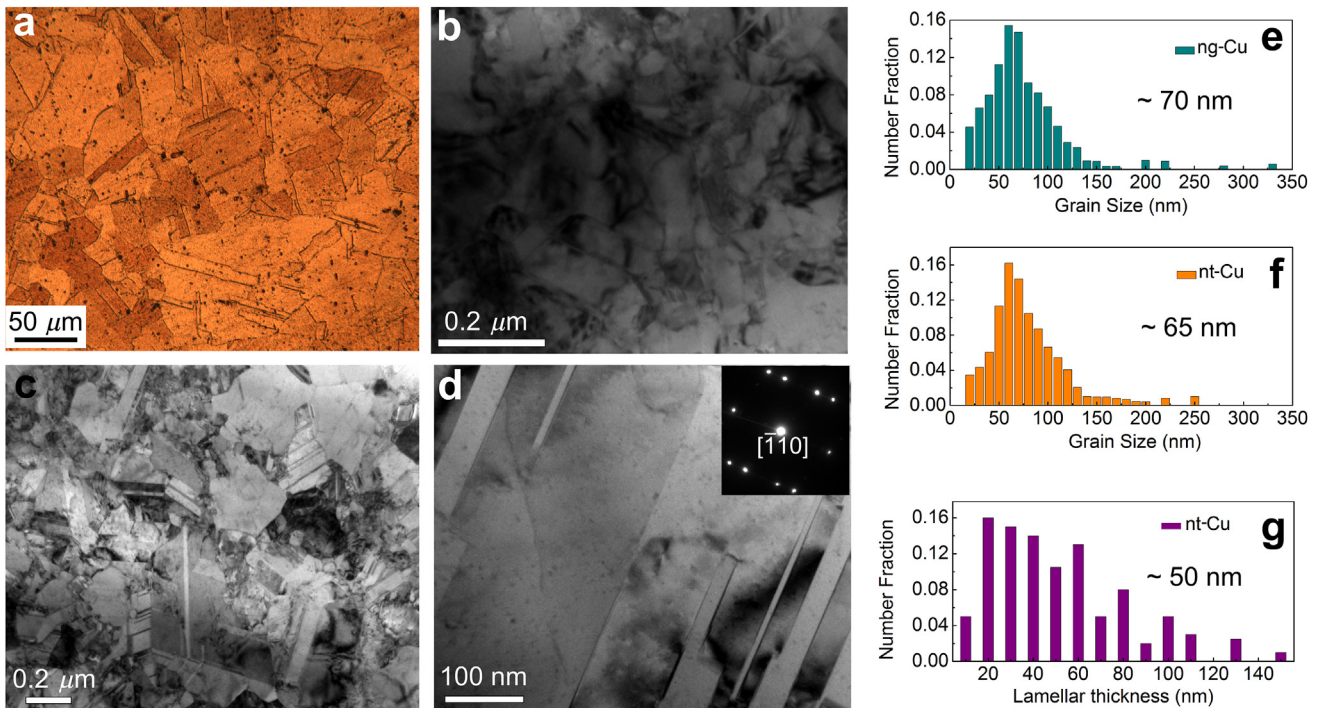


**Fig. 1.** The microstructures of the original undeformed Cu specimens. (a) The OM image of the annealing pure cg-Cu, showing the grain size of  $\sim 40 \mu\text{m}$  with some microtwins. (b–c) The representative TEM images of ng (b) and nt-Cu (c), showing many intragranular nanotwins that divide the ultrafine grains into subgrains in the nt-Cu. (d) The TEM image and the associated diffraction pattern of nanotwins indicate that nanotwins are perfectly coherent and atomically sharp without defects inside there. (e–g) The statistics columnar of the grain size in the ng-Cu (e), subgrains (f), and twin lamellar thickness (g) in the nt-Cu.

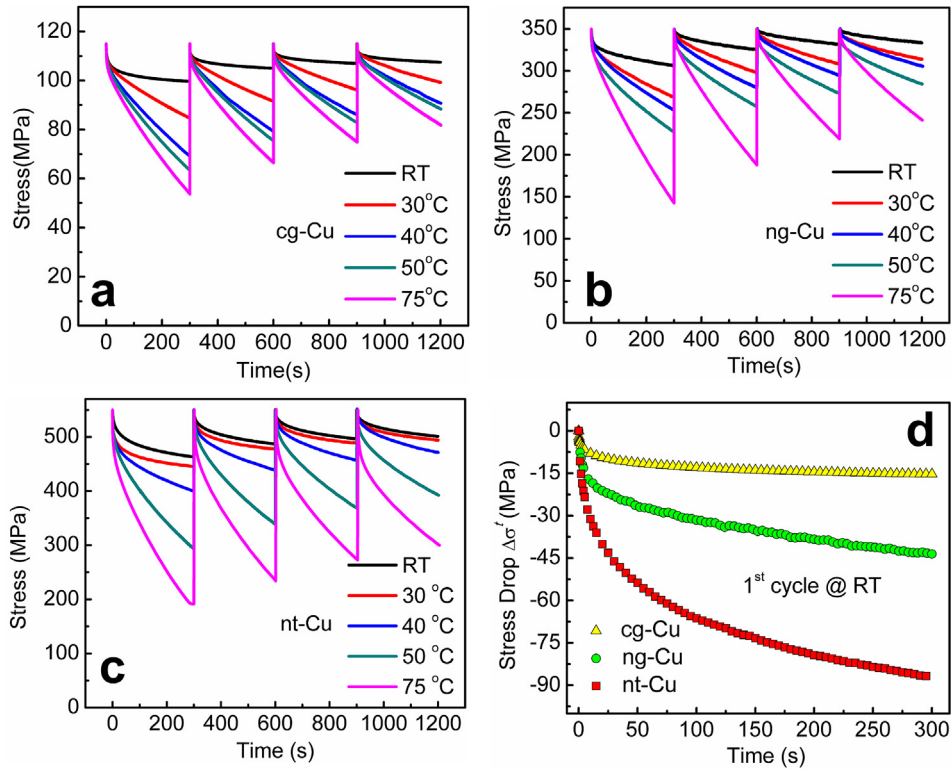


**Fig. 2.** The stress–time curves of stress relaxation on the three types of Cu specimens. (a–c) Four cycles of repeated relaxation stress–time curves of the cg, ng, and nt-Cu, respectively, at different temperatures from RT to 75 °C. (d) Comparison on the stress drop  $\Delta\sigma'$  with time in the first relaxation transient at RT for the three types of Cu specimens.

relaxation time during the first cycle of stress relaxation for the cg, ng, and nt-Cu, respectively. There are three noticeable features. 1) At a same temperature and relaxation time, the nt-Cu exhibits the highest plastic strain rate, while the cg-Cu illustrates the lowest one. 2) In the initial stage of stress relaxation, all plastic strain rates drop with relaxation time very quickly, especially in the first 20 s-relaxation. 3) After the rapidly initial decaying stage, the curves of plastic strain rate versus relaxation time exhibit absolute low slopes when the test temperatures are higher than RT, i.e., at 30 °C–75 °C, for the cg and ng-Cu and higher than 30 °C, i.e., at 40 °C–75 °C, for the nt-Cu. For example, the absolute low slopes in the 75 °C stress relaxation tests on the cg, ng, and nt-Cu are around  $1 \times 10^{-9} \text{ s}^{-2}$ ,  $3 \times 10^{-9} \text{ s}^{-2}$ , and  $9 \times 10^{-9} \text{ s}^{-2}$ , respectively. The experimental results indicate that the relaxation curves might be divided into three characteristic stages, i.e., an initial stage with rapidly drop in logarithmic strain rate, a final stage of a slightly decay in logarithmic strain rate, and a transition stage between the above two stages.

Fig. 3(d–f) illustrate the experimental data of logarithmic plastic strain rate versus stress during the first cycle of stress relaxation for the cg, ng, and nt-Cu, respectively, indicating clearly a three staged relaxation process from a linear high stress relaxation region to a subsequent nonlinear stress relaxation region and finally to a linear low stress relaxation region, which only showed-up at the test temperatures higher than 22 °C, 22 °C, and 30 °C, respectively, in the tested cg-, ng-, and nt-Cu specimens. The linear high stress relaxation region denotes the initial stage of stress relaxation, which occurs at all temperatures. The second linear region with low stresses happens in the final stage of the 300 s-stress relaxation at higher temperatures. As an example, the insets of Fig. 3(d–f) show the three staged relaxation process of the first relaxation cycle at 75 °C for the cg, ng and nt-Cu, respectively, which indicate the transition stress  $\sigma_T$  is  $\sim 100$  MPa for the cg-Cu,  $\sim 300$  MPa for the ng-Cu and  $\sim 425$  MPa for the nt-Cu. For a given stress in the transition

region, the corresponding plastic strain rate  $\dot{\epsilon}$  should be  $\dot{\epsilon} = \dot{\epsilon}_1 + \dot{\epsilon}_2$ , where  $\dot{\epsilon}_1$  and  $\dot{\epsilon}_2$  are the plastic strain rates extended from the first and second-straight line, respectively. For instance, as shown in the inset in Fig. 3(e), the strain rate  $\dot{\epsilon}$  in the ng-Cu at the stress of 287 MPa is  $\sim 6.51 \times 10^{-6} \text{ s}^{-1}$ , which is well consistent with the sum of the two strain rates:  $\dot{\epsilon}_1 \approx 1.63 \times 10^{-6} \text{ s}^{-1}$  and  $\dot{\epsilon}_2 \approx 4.9 \times 10^{-6} \text{ s}^{-1}$ . If the test temperature is low, however, the second linear region will not show up, which implies that the stress relaxation behaviors depend greatly on the test temperature. The plastic deformation in stress relaxation is attributed to the combined mechanical and thermal action, where stress is still the driving force and the relaxation is a stress-driven, and thermally-activated time-dependent process. The experimental results shown in Fig. 3(d–f) imply that in the linear high stress relaxation region, high stress causes the fast linear drop in the logarithmic strain rate against stress, where the higher the relaxation temperature is, the shorter the linear region of the logarithmic strain rate versus stress will be. In the linear low stress relaxation region, however, the logarithmic strain rate decreases slowly and linearly with decrease of stress. The different behaviors in the linear high and low stress relaxation regions might imply a switch in the deformation mechanism, which will be discussed later. The quantitative stress range in the two linear regions is estimated by the linearity of the experimental curves of logarithmic strain rate versus stress and listed in Table 1 for the first relaxation cycle.

A thermally activated process can be generally expressed by the Arrhenius relation within a certain temperature range. The plastic deformation rate,  $\dot{\epsilon}_p$ , takes the general form [28,29,32,41].

$$\dot{\epsilon}_p(\sigma, T) = \dot{\epsilon}_0(\sigma) \exp\left(-\frac{\Delta G(\sigma)}{kT}\right), \quad (2)$$

where  $\dot{\epsilon}_0(\sigma)$  is temperature-independent plastic deformation rate,

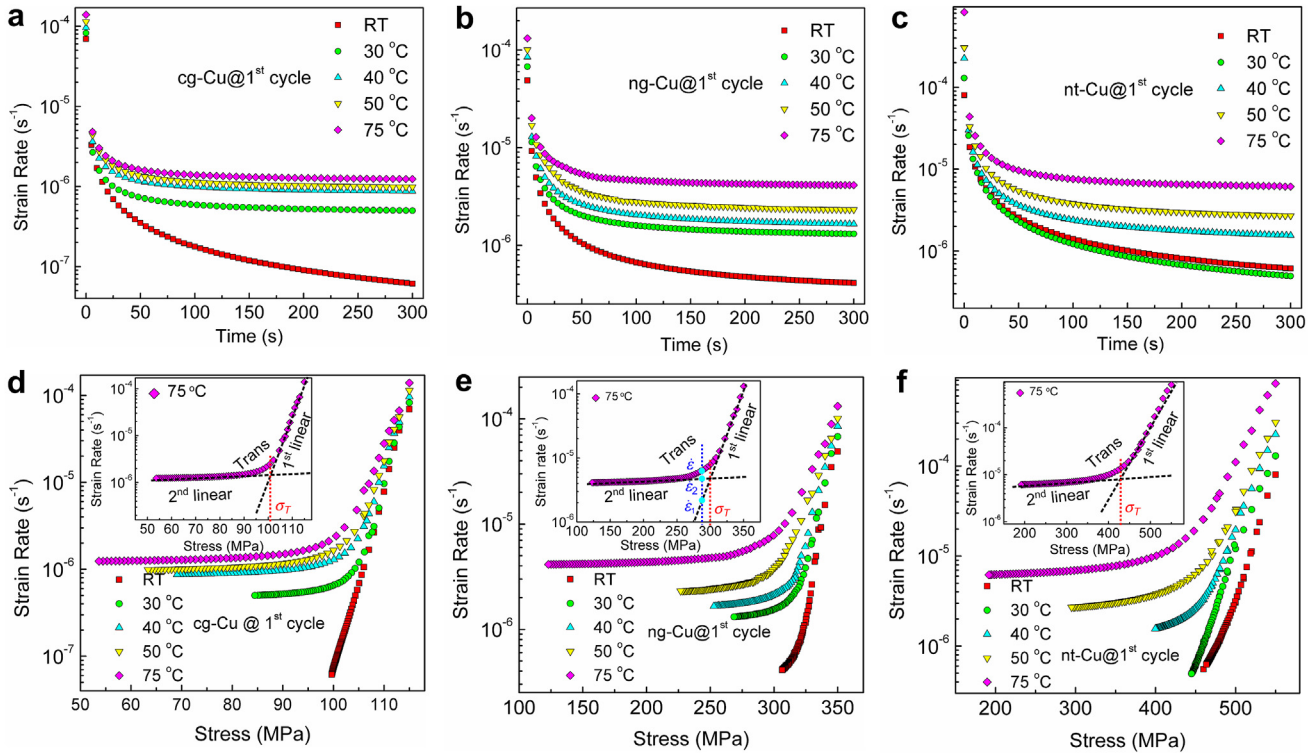


**Fig. 3.** (a–c) The curves of logarithmic strain rate versus time for the cg, ng, and nt-Cu, respectively, in the first cycle of stress relaxation. (d–f) The plots of logarithmic strain rate versus stress for the cg, ng, and nt-Cu, respectively, showing two linear stress relaxation regions and a transition region, where transition stress  $\sigma_T$  is marked in the insets for the plots at temperature 75 °C.

**Table 1**  
Stress range in the linear high and low stress relaxation regions during the first relaxation cycle.

Temperature (°C)	Linear high stress relaxation region (MPa)			Linear low stress relaxation region (MPa)		
	cg-Cu	ng-Cu	nt-Cu	cg-Cu	ng-Cu	nt-Cu
22	99 to 115	322 to 350	459 to 550	–	–	–
30	105 to 115	323 to 350	445 to 550	84 to 97	268 to 292	–
40	105 to 115	324 to 350	461 to 550	69 to 93	252 to 278	398 to 420
50	105 to 115	325 to 350	464 to 550	63 to 91	226 to 270	293 to 383
75	105 to 115	325 to 350	470 to 550	53 to 90	123 to 260	191 to 360

$\Delta G(\sigma)$  denotes apparent activation energy,  $T$  is absolute temperature,  $k$  is the Boltzmann constant. Fig. 4(a–c) show the logarithmic strain rate versus reciprocal temperature within the linear high stress relaxation region in the first cycle of stress relaxation of the cg, ng, and nt-Cu, respectively, in which the linear relationship under a given stress indicates that the Arrhenius relation of Eq. (2) holds for the stress relaxation process over the test temperature range. Therefore, according to Eq. (2), the slope and intercept yielded from the linear fitting denote the  $\Delta G(\sigma)$  and  $\ln(\dot{\epsilon}_0(\sigma))$ . The determined  $\Delta G(\sigma)$  obviously depends on the stress, as indicated by the slopes in Fig. 4(a–c). A common and simple relationship between the apparent activation energy and stress is expressed by [42–44].

$$\Delta G(\sigma) = \Delta G_0 - \sigma \tilde{V} = \Delta G_0 - \frac{\sigma}{\sqrt{3}} V, \quad (3)$$

where  $\Delta G_0$  is a stress-independent activation energy,  $\tilde{V}$  is called the tensile stress conjugated activation volume, and  $V$  is the nominal activation volume conjugated to shear stress. Note the apparent activation energy represents the overall generalized energy barrier of the tested specimens at the stress level over the test temperature

range. The tensile stress corresponded activation volume is the overall generalized activation volume in the polycrystalline specimens that the tensile stress interacts with. Since plastic deformation in metals is dominated by shear stress  $\tau$ , a relation  $\tau = \sigma/\sqrt{3}$  is commonly used with the Taylor factor of  $\sqrt{3}$ . The determined  $\Delta G(\sigma)$  is plotted against the stress in Fig. 4(d), showing that the  $\Delta G(\sigma)$  decreases almost linearly with increasing stress. The linear fitting of  $\Delta G(\sigma)$  versus stress gives  $\Delta G_0$  and  $V$  to be  $\Delta G_{0cg-1} = 3.98$  eV,  $V_{cg-1} = 607.3 b^3$  for the cg-Cu,  $\Delta G_{0ng-1} = 3.24$  eV,  $V_{ng-1} = 208.9 b^3$  for the ng-Cu, and  $\Delta G_{0nt-1} = 3$  eV,  $V_{nt-1} = 47.9 b^3$  for the nt-Cu in the linear high stress relaxation region, respectively, where  $b = 2.56$  Å is the magnitude of Burgers vector of a perfect  $1/2\langle 110 \rangle\{111\}$  dislocation in fcc-Cu.

The temperature-independent plastic deformation rate  $\dot{\epsilon}_0(\sigma)$  depends on stress and usually a power law is used to express the stress-dependent behavior, i.e. [45].

$$\dot{\epsilon}_0(\sigma) = \dot{\epsilon}_{00} \left( \frac{\sigma}{\sigma_0} \right)^n, \quad (4)$$

where  $\dot{\epsilon}_{00}$  is a stress-independent parameter,  $\sigma_0$  is a reference

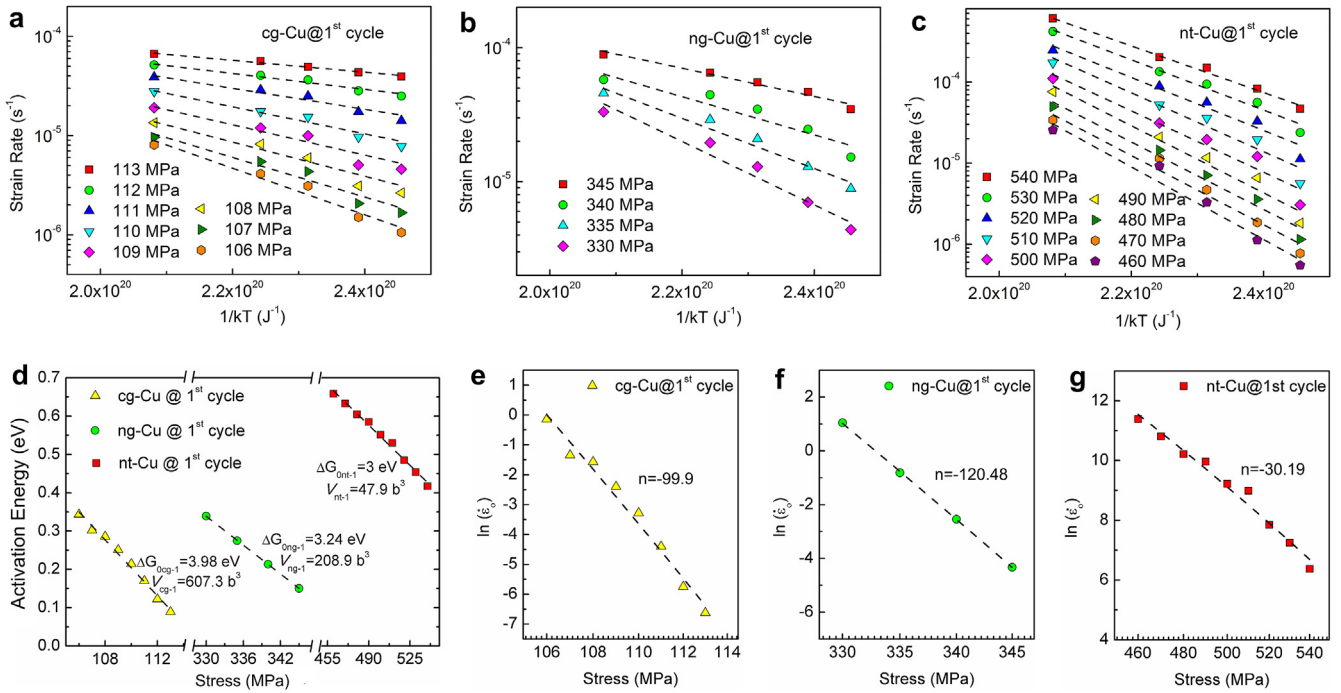


**Fig. 4.** Thermal activation parameters to be determined from the experimental data in the first linear high stress relaxation region of the first relaxation cycle. (a–c) Arrhenius plots of logarithmic strain rate against the reciprocal temperature for three types of specimens, respectively, to determine the stress-dependent activation energy and the temperature-independent plastic deformation rate. (d) The stress-dependent activation energy versus stress with linear fitting to determine the stress-independent activation energy and the activation volume. (e–g) The logarithmic temperature-independent plastic deformation rate versus logarithmic stress for the cg, ng, and nt-Cu, respectively.

stress, and  $n$  is the stress exponent. Fig. 4(e–g) are the plots of  $\ln(\dot{\epsilon}_0(\sigma))$  versus logarithmic stress, showing almost linear relationship between them. Linear fitting yields  $n = -99.9$  for the cg-Cu,  $-120.48$  for the ng-Cu, and  $-30.19$  for the nt-Cu. Obviously, the stress exponent  $n$  is negative for all the three types of specimens, which will be discussed later.

Similarly, the same method is used to determine the  $\Delta G(\sigma)$  and  $\ln(\dot{\epsilon}_0(\sigma))$  in the linear low stress relaxation region, as shown in Fig. 5(a–c). In order to illustrate the deformation characteristics in the low stress region, here the adopted stresses are as low as possible, especially at test temperatures of 40 °C, 50 °C, and 75 °C. As the stress range in the linear low stress relaxation region is very narrow at test temperatures of 40 °C, few of the strain rate versus stress data in the ng and nt-Cu are estimated from the extrapolation of the original data from Fig. 3(e, f). The Arrhenius plots in Fig. 5(a–c) show almost linear relationship between the logarithmic strain rate and the reciprocal temperature under a certain stress. The linear fitting results give that  $\Delta G(\sigma)$  varies slightly with stress, with the average value of 0.106 eV, 0.283 eV, and 0.442 eV for the cg, ng, and nt-Cu, respectively. Fig. 5(d) plots the determined  $\Delta G(\sigma)$  against stress, showing almost linear relationship and yielding the  $\Delta G_0$  and  $V$ , which are  $\Delta G_{0cg-2} = 0.11 \text{ eV}$  and  $V_{cg-2} = 0.8 \text{ b}^3$  for the cg-Cu,  $\Delta G_{0ng-2} = 0.36 \text{ eV}$  and  $V_{ng-2} = 5.05 \text{ b}^3$  for the ng-Cu, and  $\Delta G_{0nt-2} = 0.52 \text{ eV}$  and  $V_{nt-2} = 4.1 \text{ b}^3$  for the nt-Cu. Noticeably, the  $\Delta G_0$  and  $V$  in the linear low stress relaxation region are much smaller than the corresponding values in the linear high stress relaxation region. Fig. 5(e–g) show the  $\ln(\dot{\epsilon}_0(\sigma))$  versus logarithmic stress in the low stress region for the three types of specimens, respectively, indicating that  $\ln(\dot{\epsilon}_0(\sigma))$  changes slightly with stress. Linear fitting of the data with Eq. (4) gives the stress exponent  $n$ , which is closed to zero for the cg-Cu,  $-2.4$  for the ng-Cu, and  $-2.21$  for the nt-Cu. The same approach is used to analyze the measured relaxation data of the following three cycles of stress relaxation and the determined parameters are listed in Table 2.

Substituting Eqs. (3) and (4) into Eq. (2) gives the form of the Arrhenius equation,

$$\dot{\epsilon}_p(\sigma, T) = \dot{\epsilon}_0 \left( \frac{\sigma}{\sigma_0} \right)^n \exp \left( - \frac{\Delta G_0}{kT} + \frac{\sigma V}{kT\sqrt{3}} \right). \quad (5)$$

The analytic formula of plastic strain rate, i.e., Eq. (5), is built-up completely based on the experimental results. Eq. (5) is the experimentally verified strain rate equation with stress and temperature as independent parameters. The strain rate sensitivity parameter,  $m$ , reflects the strain rate dependence on stress, which is defined as:

$$m = \frac{\partial \log \sigma}{\partial \log \dot{\epsilon}} \Big|_T = \frac{\partial \ln \sigma}{\partial \ln \dot{\epsilon}} \Big|_T. \quad (6)$$

Eq. (6) indicates that the parameter  $m$  can be determined experimentally at a given temperature, which implies that the parameter  $m$  might depend on temperature. Based on Eq. (6), curves of logarithmic plastic strain rate versus logarithmic stress in the first cycle of stress relaxation are plotted for the cg, ng, and nt-Cu in Fig. 6(a–c), respectively. Surprisingly, Fig. 6(a–c) show that each curve is also consisted by two linear regions and a transition region, similar to the corresponding curve in Fig. 3(d–f), although the horizontal axis is changed from linear in Fig. 3(d–f) to logarithmic in Fig. 6(a–c). This means that the experimental data might be fitted with two different mathematic equations and each fitting has sufficient fitting accuracy, which might be caused by that logarithmic stress in the stress range of interest could be approximately expressed by a linear function of stress. The parameter  $m$  is estimated from the reciprocal of the linearly fitted slope of a linear region. For a given temperature, the value of  $m$  in the first linear high stress relaxation region is obviously smaller than that in the second linear low stress relaxation region. A large value of  $m$

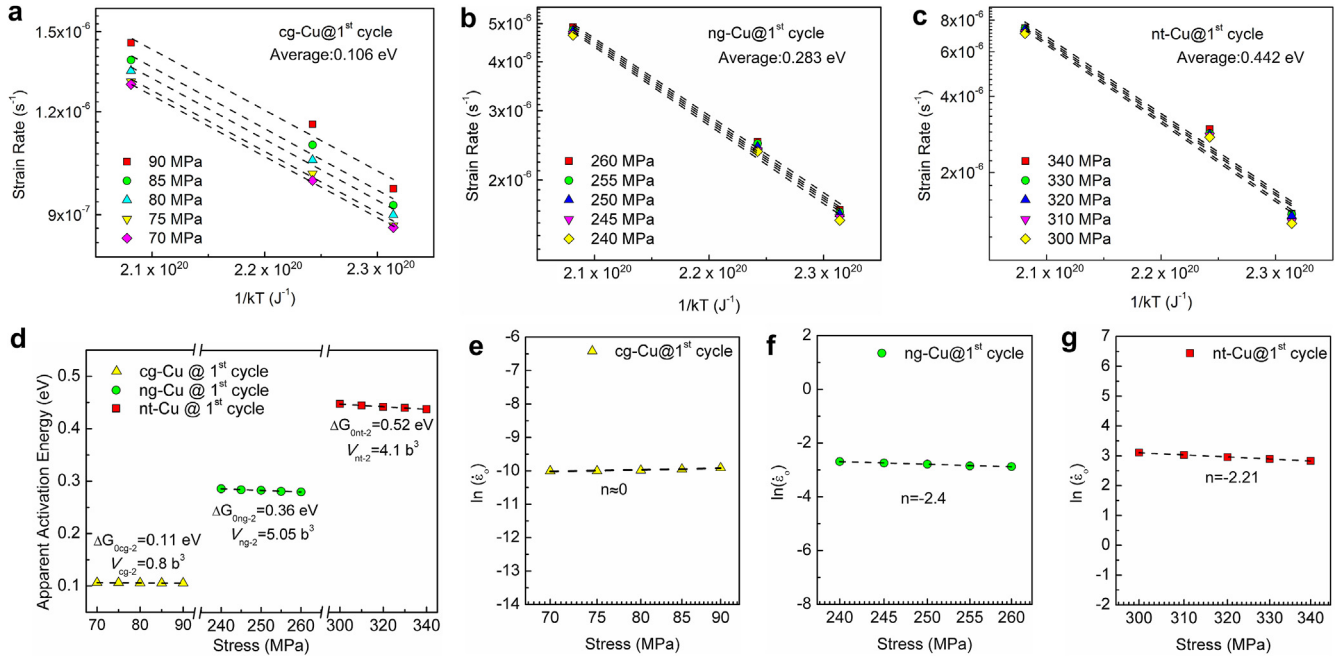


**Fig. 5.** Thermal activation parameters to be determined from the experimental data in the second linear low stress relaxation region of the first relaxation cycle. (a–c) Arrhenius plots of logarithmic strain rate against the reciprocal temperature for three types of specimens, respectively, to determine the stress-dependent activation energy and the temperature-independent plastic deformation rate. (d) The stress-dependent activation energy versus stress with linear fitting to determine the stress-independent activation energy and the activation volume. (e–g) The logarithmic temperature-independent plastic deformation rate versus logarithmic stress for the cg, ng, and nt-Cu, respectively.

**Table 2**  
The experimentally determined thermal activation parameters include the stress-independent activation energy  $\Delta G_0$ , the nominal activation volume  $V$ , and the stress exponent  $n$  in the linear high and low stress relaxation regions with the relaxation cycle number in the four cycles of repeated stress relaxation tests.

	Cycle no.	$\Delta G_0$ (eV)			$V$ ( $b^3$ )			$n$		
		cg-Cu	ng-Cu	nt-Cu	cg-Cu	ng-Cu	nt-Cu	cg-Cu	ng-Cu	nt-Cu
Linear high stress relaxation region	1st	3.97	3.24	3.03	607.3	208.9	49.7	-99.9	-120.5	-30.2
	2nd	8.37	5.78	4.48	1219.3	256.6	73.8	-210.0	-142.7	-55.5
	3rd	9.74	6.95	5.49	1392.7	309.7	104.1	-233.4	-163.8	-83.4
	4th	9.78	8.78	4.70	1404.7	633.8	85.3	-239.6	-396.6	-56.6
Linear low stress relaxation region	1st	0.110	0.36	0.52	0.80	5.05	4.1	0	-2.40	-2.21
	2nd	0.112	0.38	0.55	0.82	4.11	4.35	0	-1.37	-2.30
	3rd	0.113	0.40	0.56	0.87	4.55	3.9	0.309	-1.85	-1.61
	4th	0.115	0.43	0.58	1.12	6.23	4.23	0.446	-2.65	-1.83

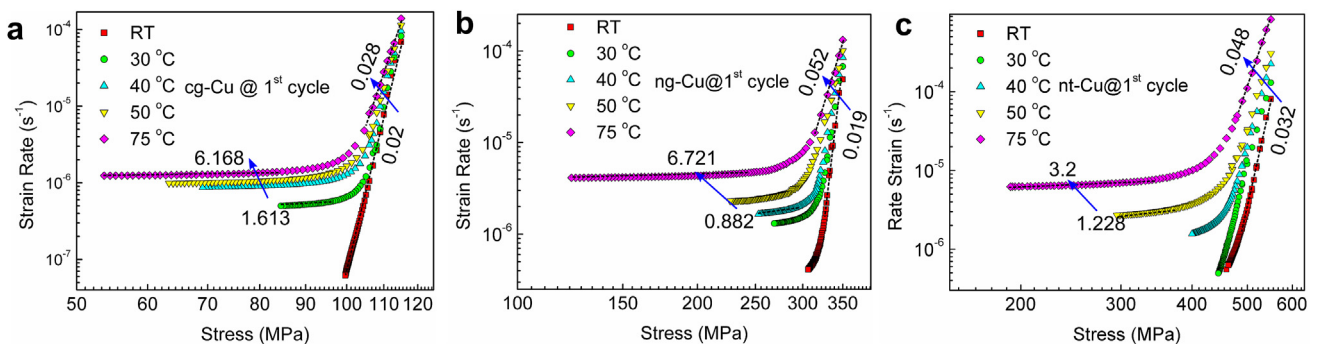


**Fig. 6.** (a, b, c) Plots of logarithmic plastic strain rate versus logarithmic stress in the first cycle of stress relaxation at different temperatures for the cg, ng, and nt-Cu, respectively, to determine the strain rate sensitivity parameter  $m$ .

indicates the superplastic behavior [46] and thus it is expected the value of  $m$  increases with temperature in either of two linear regions. For example, when temperature increases from RT to 75 °C, as indicated in Fig. 6(a–c), the value of  $m$  in the first high stress

relaxation region [linear low stress relaxation region] increases from 0.02 to 0.028 [1.613 to 6.168] for the cg-Cu, from 0.019 to 0.052 [0.882 to 6.721] for the ng-Cu, and from 0.032 to 0.048 [1.228 to 3.2] for the nt-Cu. The determined values of parameter  $m$  are all

positive, meaning that the strain rate will increase if the stress is increased. The determined values of  $n$ , however, are all negative, as described above. What is the relationship between the parameter  $m$  and the  $n$ ? From Eq. (5), the strain rate sensitivity parameter  $m$  is calculated to be:

$$\frac{1}{m} = n + \frac{\sigma V}{\sqrt{3kT}} \Big|_T \quad (7)$$

Eq. (7) indicates that the parameter  $m$  is related to the stress exponent, temperature, stress, and nominal activation volume. The experimentally determined value of  $m$  is constant within a stress range, while the term of  $\sigma V/\sqrt{3kT}$  in the right side of Eq. (7) is varied with stress. This inconsistency might be explained by the fact that the value of  $\sigma V/\sqrt{3kT}$  changes so slightly with stress in the stress range of each linear region such that the change might not be observed due to the fluctuation of the experimental data. For example, in the linear high stress relaxation region at 75 °C, substituting the activation volume gives the value of  $\sigma V/\sqrt{3kT}$  changing from 138.4 to 129.8 (average: 134.1) within the stress range from 113 MPa to 106 MPa for the cg-Cu, from 145.4 to 139 (average: 142.2) within the stress range from 345 MPa to 330 MPa for the ng-Cu, and from 52.2 to 44.4 (average: 48.3) within the stress range from 540 MPa to 460 MPa for the nt-Cu. In the linear low stress relaxation region at 75 °C, the value of  $\sigma V/\sqrt{3kT}$  are calculated to be decreased from 0.15 at 90 MPa to 0.11 at 70 MPa with average of 0.13 for the cg-Cu, from 3.13 at 260 MPa to 1.8 at 150 MPa with average of 2.54 for the ng-Cu, and from 2.81 at 340 MPa to 2.23 at 270 MPa with average of 2.52 for the nt-Cu, respectively. The validity of Eq. (7) is approved with the experimentally determined values of  $m$  and  $n$  and the average value of  $\bar{\sigma}V/\sqrt{3kT}$  in each linear region, where  $\bar{\sigma}$  is the average stress. For instance, for the linear high stress relaxation region [linear low stress relaxation region] at test temperature of 75 °C, it has  $1/m(35.5) \approx n(-99.9) + \bar{\sigma}V/\sqrt{3kT} \Big|_{75^\circ\text{C}} (134.1) [1/m(0.16) \approx n(0) + \bar{\sigma}V/\sqrt{3kT} \Big|_{75^\circ\text{C}} (0.13)]$  for the cg-Cu,  $1/m(19.22) \approx n(-120.3) + \bar{\sigma}V/\sqrt{3kT} \Big|_{75^\circ\text{C}} (142.2) [1/m(0.15) \approx n(-2.4) + \bar{\sigma}V/\sqrt{3kT} \Big|_{75^\circ\text{C}} (2.54)]$  for the ng-Cu,  $1/m(20.8) \approx n(-30) + \bar{\sigma}V/\sqrt{3kT} \Big|_{75^\circ\text{C}} (48.3) [1/m(0.31) \approx n(-2.21) + \bar{\sigma}V/\sqrt{3kT} \Big|_{75^\circ\text{C}} (2.52)]$  for the nt-Cu in the first relaxation cycle. To validate Eq. (7) with the experimentally determined properties, Table 3 lists all linear-fitted values of  $1/m$  and the calculated values of  $\bar{\sigma}V/\sqrt{3kT}$  for the two linear regions in all relaxation cycles at temperatures from RT to 75 °C for the cg, ng, and nt-Cu. Using these values, one can prove that Eq. (7) holds the relation among the strain rate sensitivity parameter, stress exponent, and nominal activation volume. The correctness of Eq. (7) alerts us that caution must be used in the determination of nominal activation volume if stress relaxation tests are conducted at only a given temperature.

### 3.2. MD simulations of stress relaxation

Fig. 7(a, e) are the stress-strain relaxation curves at 300 K, 500 K, and 800 K for the ng-Cu and nt-Cu, respectively, showing that the nt-Cu exhibits a higher flow stress at a given temperature than its twin-free counterpart. Fig. 7(b, f) and insets illustrate the curves of logarithmic strain rate versus time and stress versus time, respectively. As expected, the higher the temperature is, the faster the stress drops and the more quickly the plastic strain rate falls with time. In the Supplementary material, Fig. S2 (a–c) show the stress drop versus time of the simulated nt and ng samples at temperatures of 300 K, 500 K, and 800 K, respectively. The nt sample exhibits enhanced stress drop at 300 K and 500 K, while the ng and nt samples illustrate quite similar stress relaxation behaviors at 800 K.

This might indicate the deformation mechanism at 800 K is quite different from that at low temperatures of 300 K and 500 K. Fig. 7(c, g) and insets plot the curves of logarithmic plastic strain rate versus logarithmic stress and logarithmic plastic strain rate versus stress, respectively, for simulated ng- and nt-Cu. There is only one linear region at 300 K or 500 K, while a linear region plus a nonlinear transition region appears at 800 K. The simulation duration is not long enough, especially at 300 K and 500 K, so that the transition in the deformation behavior observed in experiments does not appear at the relatively low simulation temperatures. The determined  $m$  values are 0.04, 0.068, and 0.164 for the ng-Cu, and 0.041, 0.071, and 0.147 for the nt-Cu, respectively, at temperatures of 300 K, 500 K, and 800 K. The results are consistent with these experimental values in the linear high stress relaxation regions shown in Table 3. The apparent activation energy could not be obtained by fitting the Arrhenius plots, because no strain rates at equal-stress were found in the MD simulations. Based on Eq. (7), the reciprocal of strain rate sensitivity parameter of  $1/m$  is plotted against the team of  $\bar{\sigma}/kT$  with  $\bar{\sigma}$  being the average stress within a given linear region in Fig. 7(d, h) respectively for the ng and nt-Cu. The activation volume  $V$  and stress exponent  $n$  are respectively estimated from the slope and interception of the plots in Fig. 7(d, h) by linear fitting. The determined values of  $V$  and  $n$  are 6.15 b<sup>3</sup> and 2.059 for the ng-Cu, and 5.08 b<sup>3</sup> and 3.129 for the nt-Cu. Compared to the experimental results in the linear high stress relaxation regions, the MD simulations give the corresponding smaller activation volume, which might be due to the smaller length scale, such as grain size and twin spacing, used in the MD simulations. A smaller activation volume makes the apparent energy is much less sensitive to stress. In this case, the influence of stress on the relaxation process is mainly contributed by the stress exponent  $n$ , which becomes positive in the MD simulations, rather than negative in the experiments.

## 4. Discussion

### 4.1. Deformation parameters

The experimentally determined deformation parameters include strain rate sensitivity parameter  $m$ , stress exponent  $n$ , and activation volume  $V$  in the linear high- and low-stress relaxation regions are all listed in Tables 2 and 3 for all relaxations cycles, and confirm the validity of Eq. (7). Researchers might be often confused between the  $m$  and the  $n$ , especially in treating isothermal stress relaxation data obtained at only a certain temperature. This is because that the apparent activation energy under a given stress level requires experimental data at various temperatures, as illustrated in the present work. Therefore, it is a must to carry out stress relaxation tests at various temperatures. As indicated in Eq. (7),  $1/m$  will equal  $n$ , only when  $V$  approaches zero. The strain rate sensitivity reflects the stress contribution to the plastic strain rate and the stress contribution is executed by lowering the apparent activation energy via thermal excitation and by increasing the athermal stress effect represented by the stress exponent. Thus, for a given  $m$ ,  $n$  might be positive or negative depending on the value of  $V$ , which has been illustrated by the experimental and simulation results.

The fact that the experimental data under a given stress at various temperatures can be perfectly expressed by the Arrhenius plots of logarithmic plastic strain rate versus reciprocal temperature indicates that 1) the stress-dependent apparent activation energy can be approximately treated as a constant over a certain temperature range of interest, and 2) the temperature affects the relaxation behavior only via the stress-dependent apparent activation energy. The stress-dependent apparent activation energy is

**Table 3**  
The reciprocal of strain rate sensitivity parameter  $1/m$  and the calculated average value of  $\sigma V/\sqrt{3}kT(1/m)/\sigma V/\sqrt{3}kT$  in the linear high and low stress relaxation regions for the cg, ng and nt-Cu, respectively, at temperatures of RT, 30 °C, 40 °C, 50 °C, and 75 °C in the four relaxation cycles.

Relax no.	Temperature (°C)	Linear high stress relaxation region			Linear low stress relaxation region		
		cg-Cu	ng-Cu	nt-Cu	cg-Cu	ng-Cu	nt-Cu
1st cycle	22	49.4/153.0	53.4/167.8	31.1/57.0	–	–	–
	30	54.3/150.0	39.8/162.1	27.3/55.4	0.62/0.18	–	–
	40	44.5/145.7	32.1/156.9	25.7/53.7	0.24/0.16	1.13/3.37	–
	50	42.0/142.5	24.7/152.0	23.1/52.0	0.23/0.14	0.75/3.23	0.78/3.03
	75	35.5/134.1	19.2/142.2	20.8/48.3	0.16/0.13	0.15/2.54	0.31/2.52
2nd cycle	22	119.5/319.1	70.8/207.6	43.0/93.1	–	–	–
	30	102.9/310.7	58.4/202.1	40.6/90.6	–	–	–
	40	74.0/300.8	48.8/195.7	37.3/87.7	0.42/0.16	0.89/2.32	–
	50	68.3/291.5	–	29.5/85.0	0.29/0.14	0.88/1.99	0.81/3.33
	75	56.6/270.5	30.3/175.9	22.6/78.9	0.23/0.13	0.25/1.65	0.36/2.63
3rd cycle	22	136.0/367.0	106.4/257.2	50.1/130.3	–	–	–
	30	112.3/358.1	90.3/254.0	44.8/127.8	–	–	–
	40	–	–	41.6/123.8	0.67/0.17	1.26/3.06	–
	50	85.1/335.9	64.9/228.8	34.9/119.9	0.51/0.15	1.22/2.86	0.99/2.88
	75	61.3/311.8	45.5/212.4	25.2/111.3	0.40/0.11	0.37/2.42	0.54/2.18
4th cycle	22	143.8/372.7	119.0/512.8	54.9/106.6	–	–	–
	30	116.2/362.8	94.7/499.2	44.0/103.7	–	–	–
	40	97.3/351.2	87.5/483.3	40.3/100.4	0.72/0.24	1.61/4.33	–
	50	90.4/340.4	72.1/468.3	37.9/97.3	0.59/0.22	1.44/4.06	1.48/3.49
	75	78.0/315.9	–	28.2/91.2	0.54/0.14	0.51/3.27	0.82/3.07

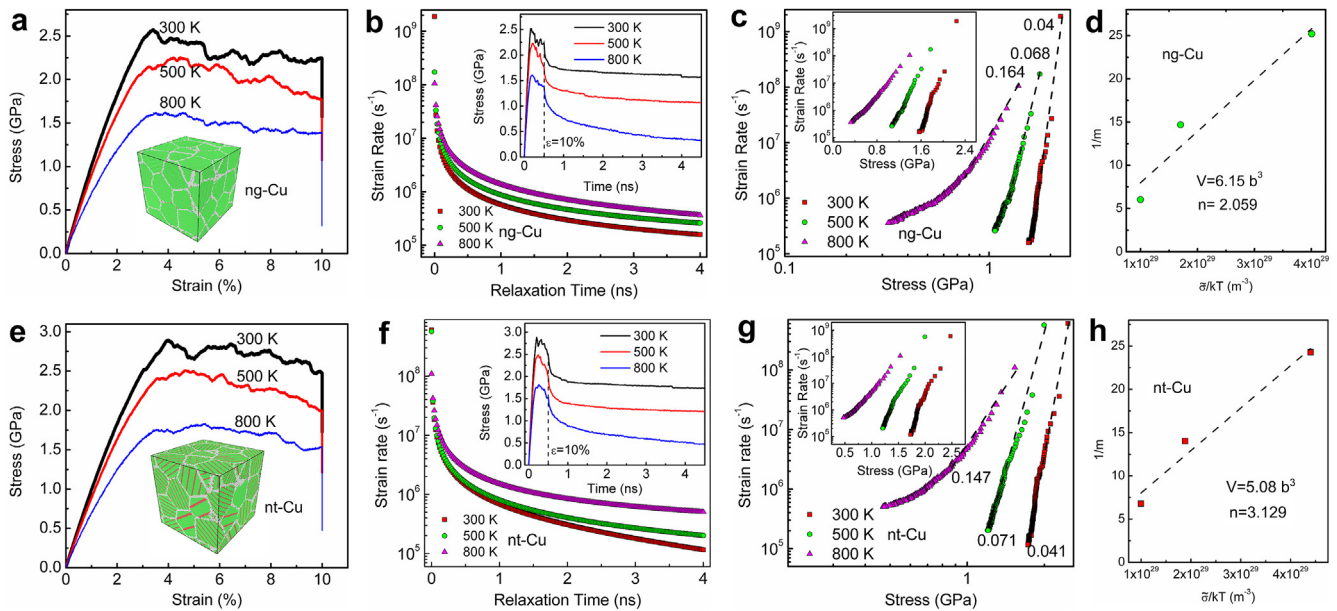


**Fig. 7.** The MD simulations of stress relaxation. (a, e) The stress–strain curves at 300 K, 500 K, and 800 K of the simulated ng- and nt-Cu specimens, respectively, where the insets represent the atomic models of the ng- and nt-Cu. The grain size in the simulated ng- and nt-Cu is 10 nm, and the twin lamellar is 1.25 nm in the simulated nt-Cu. (b, f) The logarithmic strain rate versus time curves at different temperatures of the simulated ng- and nt-Cu, respectively, where the corresponding insets plot the stress versus time curves. (c, g) The logarithmic strain rate versus logarithmic stress of the simulated ng- and nt-Cu, respectively, where the insets show the corresponding curves of logarithmic strain rate versus stress. (d, h) The reciprocal of strain rate sensitivity parameter versus the term of  $\sigma/kT$  at various temperatures for the ng and nt-Cu, respectively.

reduced from the stress-independent intrinsic activation energy by the mechanical work, i.e., the product of stress times activation volume, as indicated in Eq. (3). Thus, the activation volume is independent of temperature over the studied temperature range in the present investigations. But the magnitude of activation volume is highly related to the flow stress level, as listed in Table 2. In dislocation-mediated plasticity, a high yield strength with working hardening of a material indicates a high resistance of the material against large scale dislocation nucleation and motion. Fig. S1(a) indicates that the RT yield strengths of the cg-, ng-, and nt-Cu are  $\sim 75$  MPa,  $\sim 300$  MPa, and  $\sim 420$  MPa, respectively. A high yield

strength corresponds high flow stresses in the first linear high stress relaxation region, as indicated in Table 1. In the linear high stress relaxation region, the higher the flow stress level is, the smaller activation volume will be. It is shown in Table 2 that the activation volumes in the linear high stress relaxation region of the first relaxation cycle are  $607.3 b^3$ ,  $208.9 b^3$ , and  $49.7 b^3$ , respectively, for the cg-, ng-, and nt-Cu. Thus, we may have the correlation that in dislocation-mediated plasticity, the higher the yield strength is, the smaller the activation volume will be. Once the deformation mechanism changes, the activation volume will also change. Therefore, the activation volumes in the linear high stress

relaxation regions are obviously larger than those corresponding ones in the linear low stress relaxation regions. For example, the nt-Cu during the first relaxation cycle possesses the activation volume of  $47.9 b^3$  in the linear high stress relaxation region and a much lower value of activation volume  $4.1 b^3$  in the linear low stress relaxation region, which indicates the change in deformation mechanism.

The activation volume and activation energy are signatures of the thermally active deformation mechanism. The activation volume may represent a generalized area swept by a perfect dislocation during the thermally activated process. Thus, taking the first relaxation cycle as an example, the swept areas in the linear high stress relaxation region are  $39.8 (\text{nm})^2$ ,  $13.7 (\text{nm})^2$ , and  $3.1 (\text{nm})^2$  in the cg, ng, and nt-Cu, respectively, which is expected because the GBs and TBs impede dislocation motion and the nt-Cu possess the tiniest subgrain size. Provided that the perfect dislocation sweep mechanism is still valid, the swept areas in the linear low stress relaxation region are surprisingly reduced to  $0.05 (\text{nm})^2$ ,  $0.33 (\text{nm})^2$ , and  $0.27 (\text{nm})^2$  in the cg, ng, and nt-Cu, respectively, which are too small to believe that the perfect dislocation sweep mechanism. Alternately, it suggests the deformation mechanism of atomic diffusion, GB/TB movement, or/and partial dislocation activity. It is generally accepted that dislocation-mediated plastic deformation gives a large activation volume at the order of several hundred  $b^3$  and above, while GB diffusion mediated creep (Coble creep) possesses a small activation volume, less than  $1 b^3$ . Dislocation cross-slip or/and dislocation nucleation might be associated with the activation volume ranging from several  $b^3$  to  $100 b^3$  [4,10,11,14,16–18,23–25,28,32,47,48]. On the other hand, dislocation-mediated plastic deformation entails an activation energy larger than 1 eV, while is lower than 1 eV for boundary-associated deformation [28,29,49–52]. Therefore, the observed variations in the stress-independent activation energy and in the activation volume indicate the deformation mechanism transition with the decrease of flow stress, i.e., from the dislocation activity-dominated deformation in the linear high stress relaxation region to the boundary-associated deformation in the linear low stress relaxation region. In details, in the linear high stress relaxation regions, the dislocation activity-dominated deformation might be the cutting forest dislocations in the cg-Cu, reflected by the largest activation volume, while the dislocation interaction with the GBs and TBs in the ng and nt-Cu might yield the smaller activation volume. In the linear low stress relaxation regions, the Coble creep mechanism is predominant in the cg-Cu, as indicated by the lowest activation energy and the smallest activation volume less than  $1 b^3$ . The activation volume is around  $5 b^3$  in both the ng and nt-Cu and the activation energy is about 0.3 eV in the ng-Cu and 0.5 eV in the nt-Cu, which might be related to other boundary-associated mechanisms. For the ng-Cu, the mechanism might be GB sliding [12–14], or/and grain rotation [15]. However, the TBs sliding and twin rotation becomes almost impossible in the nt-Cu due to the highly coherent atomic planes of TBs [22].

Eq. (5) shows that the mechanical work ( $\sigma V$ ) lowers the energy barrier. The values of apparent activation energy are about one order lower in magnitude than those of the stress-independent activation energy  $\Delta G_0$  in the linear high stress relaxation region, as shown in Fig. 4(d), meaning that more mobile dislocations are fully activated due to the sufficiently high mechanical work. In the linear low stress relaxation region shown in Fig. 5(d), the deformation mechanism must have the feature that possesses a small value of  $\Delta G_0$  due to the low stress. Thus, a low stress associated with a small activation volume can also activate the diffusional process. Although the nominal apparent activation energies in the two linear regions are comparable, the plastic strain rates in the linear high stress relaxation region are evidently higher than those

in the linear low stress relaxation region, as revealed in Figs. 3–5. To achieve this difference in plastic strain rate, the stress-independent prefactor  $\dot{\epsilon}_{00}$  is changed associated with the transition of deformation mechanism. The prefactor depends on the grain size/twin spacing, i.e.,  $\dot{\epsilon}_{00} \propto (1/d)^p$ , where  $d$  is the grain size/twin spacing, and the  $p$  is the grain size exponent [45]. Normally,  $p$  is characterized to be one for dislocation activity and three for GB diffusion. Therefore, the much larger  $\dot{\epsilon}_{00}$  and the mechanical work in the linear high stress relaxation region results in the obviously higher plastic strain rates than those in the linear low stress relaxation region. On the other hand, the largest  $\dot{\epsilon}_{00}$  in the nt-Cu due to the finest length scale can also effectively denote the highest plastic deformation strain rate among all three types of specimens in each given relaxation stage, as shown in Fig. 4(d) and Fig. 5(d), even though the apparent activation energies in the nt-Cu are largest. As listed in Table 2, the activation energies increase with the relaxation cycle, meaning that the thermal activated plastic deformation becomes more and more difficult, which is supported by the experiment results that the total stress drop decreases with the increase of relaxation cycles at a given temperature.

In comparison with the cg and ng-Cu, the nt-Cu still exhibits the most significant total stress drop, or the highest plastic strain rates, at the same temperature and the same relaxation cycle, which are attributed to the nt structure. It is difficult for dislocations to accumulate and pile-up in the interior of nanometer size grains in the ng metals, and alternatively, deformation behavior associated to GBs becomes dominant. Of course, there are wide-awake of dislocation sources near random GBs where dislocations can nucleate readily. These GB sources are not regenerative and might be exhausted instantly upon straining [30,53,54]. Mobile dislocations are also very easy to annihilate at GBs. If no more straining is applied, the number of mobile dislocations will decrease quickly in the ng specimens. In contrast, the TB-mediated dislocation slip-transfer reactions in the nt specimens will more effectively promote dislocation nucleation and motion. Studies [5,6,25,55–57] show that interactions between dislocations and TBs in nt materials may result in glissile dislocations along TBs (i.e. twinning partials), sessile dislocations or locks at TBs, and/or outgoing dislocations or stacking faults in the neighboring twin planes, depending upon the nature of incoming reactant dislocations. Coherent TBs can readily trap and absorb lattice dislocations. HRTEM images [57] show the double functions of TBs, as barriers against dislocation motion and dislocation sources as well. Dislocations accumulated on TBs can remain mobile or/and change to dislocation sources because of the TB coherency. Thus, high density of dislocations can easily glide along TBs to accommodate subsequent deformation, especially after reloading in the repeated stress relaxation tests.

#### 4.2. MD simulation and HRTEM observations

Fig. S3 in the Supplementary material indicates that coherent TBs pin the GBs, and thereafter suppress the boundary-associated rotation, migration and diffusion mechanism. Fig. 8 (a, c) are MD snapshots of the nt-Cu stress-relaxed at 300 K for 4 ns, while Fig. 8 (b, d) show the associated stress maps respectively. Dislocations nucleated from the TBs may glide along slip planes inclined and parallel to the TBs and the dislocations are called inclined and parallel dislocations correspondingly. Stress concentration occurs usually at intersections of GBs and TBs, as shown in Fig. 8 (b, d), and the highly stress-concentrated intersections are the potential dislocation nucleation sites. As mentioned above, TBs may block inclined dislocations and high stress is accompanied with dislocations. Fig. 8 (b, d) show also the dislocation high stress locations, which are at the intersections of inclined dislocations and TBs. The

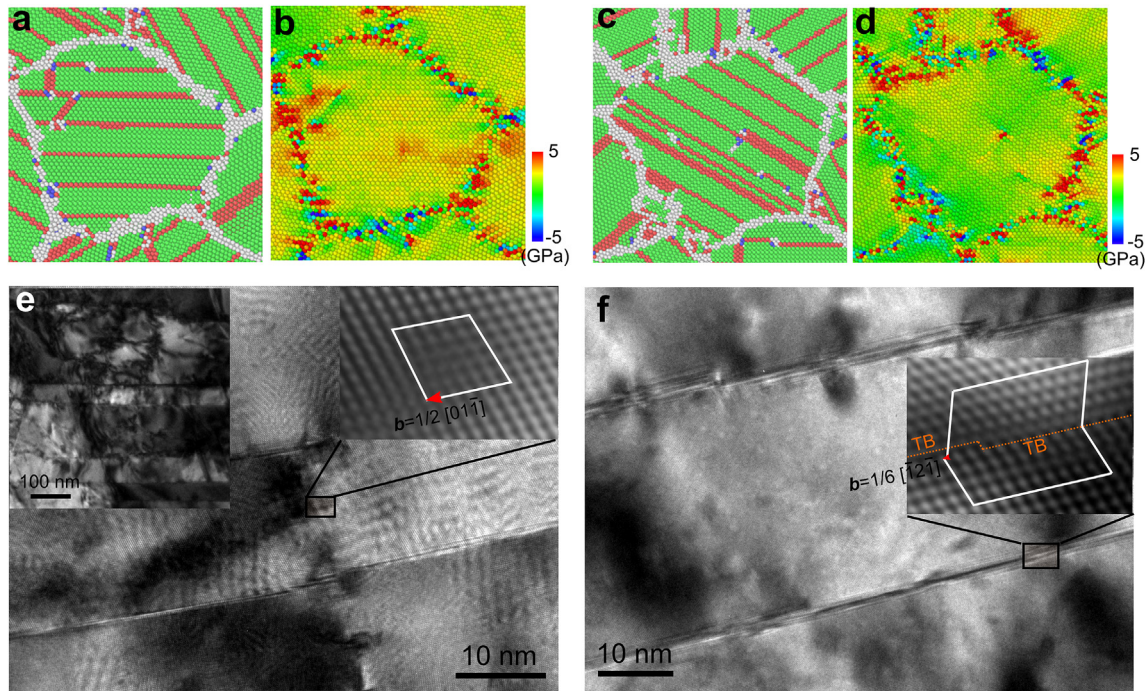


**Fig. 8.** (a–d) The snapshots and associated stress maps of the simulated nt-Cu relaxed at 300 K, showing the inclined dislocation (a, b) and the parallel dislocation (c, d), where the stress color-bar is scaled from  $-5$  GPa to  $5$  GPa. (e–f) HRTEM images of the experimentally relaxed nt specimens, showing the inclined perfect dislocation pile-up and cutting through the twin plane at RT (e) and the parallel Shockley partial dislocation nucleation and motion along the twin plane resulting in the twinning or de-twinning at  $75$  °C (f). The atoms in (a, c) are colored according to their CNA with fcc in green, hcp (stacking fault or twin boundaries) in red, and disordered atoms in white. (For interpretation of the references to color in this figure legend, the reader is referred to the web version of this article.)

Shockley partial dislocations may be nucleated from the intersections of GBs and TBs and then move on the TBs and neighboring planes with the same slip system. The nucleation and movement of Shockley partial dislocations are actually the twinning and detwinning processes, as illustrated in Fig. 8(c). Zhu. et al. [25] demonstrated the similar transmission process of the inclined and partial dislocations including the absorption process to TBs and the desorption process from TBs by MD simulations. Note that stress concentration is also observed along GBs in the ng sample, as shown in Fig. S4 in the Supplementary material, which triggers the GB dislocation nucleation. Comparing Fig. S4 with Fig. 8(a–d) indicates the similarity that GBs are high stress locations in both simulated ng and nt samples. In the nt sample, dislocations, especially parallel dislocations, are easily nucleated from the TB/GB intersections, while in the ng sample, dislocations are nucleated from the highly stress GBs. The GB dislocation nucleation sites in the ng sample could be closely associated with the local atom arrangement inside the GBs, which deserves further investigation, while in the nt sample the TB/GB intersections are unambiguously the geometrically and energetically favored dislocation nucleation sites. In addition to the MD simulation results, inclined and parallel dislocations are observed by HRTEM on the nt-Cu stress-relaxed at RT and  $75$  °C, as shown in Fig. 8(e, f), respectively. The dislocation mediated plasticity is dominated in the RT relaxation via perfect inclined dislocation pile-up and cut through TBs, as indicated by the Burger vector of an inclined dislocation indexed in the inset of Fig. 8(e). Fig. 8(f) shows the Shockley partial dislocations nucleated and moving along TBs, leading to TB migration. The findings of both inclined and parallel dislocations from the MD simulations and HRTEM observations are in perfect agreement with a recently proposed theory about the dislocation-nucleation-governed strengthening and softening in nt metals [22].

## 5. Concluding remarks

The formula of Eq. (5) describing the time, stress, and temperature-dependent deformation is built up based on the experimental results of the stress relaxation tests on the cg-, ng-, and nt-Cu at  $22$  °C (RT),  $30$  °C,  $40$  °C,  $50$  °C, and  $75$  °C. The critical step to achieve this formula is to have sufficient data of plastic deformation rate at various temperatures under a certain stress level and the experimental data can be perfectly expressed by the Arrhenius plots of logarithmic plastic strain rate versus reciprocal temperature. Thus, the stress-dependent apparent activation energy can be approximately treated as a constant over a certain temperature range of interest and the temperature affects the relaxation behavior only via the stress-dependent apparent activation energy. Then, the stress-independent activation energy and the activation volume are naturally temperature-independent properties in the temperature range of study. In dislocation-mediated plasticity, a high yield strength corresponds high flow stresses in the first linear high stress relaxation region, in which the higher the flow stress level is, the smaller activation volume will be. Once the deformation mechanism changes, the activation volume will also change. Therefore, the activation volumes in the linear high stress relaxation regions are obviously larger than those corresponding ones in the linear low stress relaxation regions. From Eq. (5), it is straightforward to clarify the relationship among the strain rate sensitivity parameter, stress exponent, and activation volume. The strain rate sensitivity parameter is often used to gage the stress contribution to the plastic strain rate when stress relaxation tests are conducted at only a temperature. As illustrated in the present work, the stress contribution to the plastic strain rate is done through two channels, 1) lowering the stress-independent activation energy by doing the mechanical work with its thermodynamic conjugate of activation volume, and 2) varying the athermal stress function by changing the

value of stress exponent. Only when the value of activation volume approaches zero, the reciprocal of strain rate sensitivity parameter equals approximately to the stress exponent.

## Acknowledgments

This work was supported by the General Research Fund (Project number, 622911) from the Hong Kong Research Grants Council. T.Y.Z. is grateful for the financial support by the research grant (No.14DZ2261200) from the Science and Technology Commission of Shanghai Municipality. Y.J.W and L.H.D acknowledge the financial supports from the NSFC (Nos. 11132011, 11402269, 11472287), the National Key Basic Research Program of China (No. 2012CB937500), and the CAS/SAFEA International Partnership Program for Creative Research Teams. G.Y. W thanks the National Nature Science Foundation (grant No. 51401083).

## Appendix A. Supplementary data

Supplementary data related to this article can be found at <http://dx.doi.org/10.1016/j.actamat.2016.02.021>.

## References

- [1] E.O. Hall, The deformation and ageing of mild steel: III discussion of results, *Proc. Phys. Soc. Sec. B* 64 (1951) 747.
- [2] N.J. Petch, The cleavage strength of polycrystals, *J. Iron Steel Inst.* 174 (1953) 25–27.
- [3] L. Lu, Y. Shen, X. Chen, L. Qian, K. Lu, Ultrahigh strength and high electrical conductivity in copper, *Science* 304 (2004) 422–426.
- [4] M. Dao, L. Lu, Y.F. Shen, S. Suresh, Strength, strain-rate sensitivity and ductility of copper with nanoscale twins, *Acta Mater* 54 (2006) 5421–5432.
- [5] Z.H. Jin, P. Gumbsch, E. Ma, K. Albe, K. Lu, H. Hahn, H. Gleiter, The interaction mechanism of screw dislocations with coherent twin boundaries in different face-centred cubic metals, *Scr. Mater* 54 (2006) 1163–1168.
- [6] Z.H. Jin, P. Gumbsch, K. Albe, E. Ma, K. Lu, H. Hahn, H. Gleiter, Interactions between non-screw lattice dislocations and coherent twin boundaries in face-centered cubic metals, *Acta Mater* 56 (2008) 1126–1135.
- [7] J. Schiøtz, T. Vegge, F.D. Di Tolla, K.W. Jacobsen, Atomic-scale simulations of the mechanical deformation of nanocrystalline metals, *Phys. Rev. B* 60 (1999) 11971–11983.
- [8] Y. Kulkarni, R.J. Asaro, Are some nanotwinned fcc metals optimal for strength, ductility and grain stability? *Acta Mater* 57 (2009) 4835–4844.
- [9] V. Yamakov, D. Wolf, S.R. Phillpot, A.K. Mukherjee, H. Gleiter, Deformation-mechanism map for nanocrystalline metals by molecular-dynamics simulation, *Nat. Mater* 3 (2004) 43–47.
- [10] G. Wang, J. Lian, Z. Jiang, L. Qin, Q. Jiang, Compressive creep behavior of an electric brush-plated nanocrystalline Cu at room temperature, *J. Appl. Phys.* 106 (2009) 086105.
- [11] Z. Jiang, X. Liu, G. Li, Q. Jiang, J. Lian, Strain rate sensitivity of a nanocrystalline Cu synthesized by electric brush plating, *Appl. Phys. Lett.* 88 (2006) 143115.
- [12] J. Schiøtz, K.W. Jacobsen, A maximum in the strength of nanocrystalline copper, *Science* 301 (2003) 1357–1359.
- [13] H.V. Swygenhoven, Polycrystalline materials: grain boundaries and dislocations, *Science* 296 (2002) 66–67.
- [14] Z. Jiang, H. Zhang, C. Gu, Q. Jiang, J. Lian, Deformation mechanism transition caused by strain rate in a pulse electric brush-plated nanocrystalline Cu, *J. Appl. Phys.* 104 (2008) 053505.
- [15] Z. Shan, E.A. Stach, J.M.K. Wiezorek, J.A. Knapp, D.M. Follstaedt, S.X. Mao, Grain boundary-mediated plasticity in nanocrystalline nickel, *Science* 305 (2004) 654–657.
- [16] X. Shen, C. Gu, J. Lian, Q. Jiang, Z. Jiang, L. Qin, Tensile-relaxation behavior of electrodeposited nanocrystalline Ni, *J. Appl. Phys.* 108 (2010) 054319.
- [17] X. Shen, C. Zhang, T. Zeng, D. Cheng, J. Lian, Understanding the microscopic deformation mechanism and macroscopic mechanical behavior of nanocrystalline Ni by the long-term stress relaxation test, *Int. J. Mod. Phys. B* 28 (2014) 1450124.
- [18] Y.-J. Wang, A. Ishii, S. Ogata, Transition of creep mechanism in nanocrystalline metals, *Phys. Rev. B* 84 (2011) 224102.
- [19] X. Zhang, A. Misra, Superior thermal stability of coherent twin boundaries in nanotwinned metals, *Scr. Mater* 66 (2012) 860–865.
- [20] S. Zheng, I.J. Beyerlein, J.S. Carpenter, K. Kang, J. Wang, W. Han, N.A. Mara, High-strength and thermally stable bulk nanolayered composites due to twin-induced interfaces, *Nat. Commun.* 4 (2013) 1696.
- [21] J. Bezarek, S. Jiao, Y. Liu, D. Bufford, L. Lu, X. Zhang, Y. Kulkarni, R.J. Asaro, Indentation of nanotwinned fcc metals: implications for nanotwin stability, *Acta Mater* 60 (2012) 4623–4635.
- [22] X. Li, Y. Wei, L. Lu, K. Lu, H. Gao, Dislocation nucleation governed softening and maximum strength in nano-twinned metals, *Nature* 464 (2009) 877–880.
- [23] Y.M. Wang, E. Ma, Temperature and strain rate effects on the strength and ductility of nanostructured copper, *Appl. Phys. Lett.* 83 (2003) 3165–3167.
- [24] M. Dao, L. Lu, R.J. Asaro, J.T.M. De Hosson, E. Ma, Toward a quantitative understanding of mechanical behavior of nanocrystalline metals, *Acta Mater* 55 (2007) 4041–4065.
- [25] T. Zhu, J. Li, A. Samanta, H.G. Kim, S. Suresh, Interfacial plasticity governs strain rate sensitivity and ductility in nanostructured metals, *Proc. Nat. Acad. Sci.* 104 (2007) 3031–3036.
- [26] T. Zhu, H. Gao, Plastic deformation mechanism in nanotwinned metals: an insight from molecular dynamics and mechanistic modeling, *Scr. Mater* 66 (2012) 843–848.
- [27] J.F. Chen, J.T. Jiang, L. Zhen, W.Z. Shao, Stress relaxation behavior of an Al-Zn-Mg-Cu alloy in simulated age-forming process, *J. Mater. Proc. Tech.* 214 (2014) 775–783.
- [28] Y.M. Wang, A.V. Hamza, E. Ma, Temperature-dependent strain rate sensitivity and activation volume of nanocrystalline Ni, *Acta Mater* 54 (2006) 2715–2726.
- [29] D. Caillard, J.-L. Martin, *Thermally Activated Mechanisms in Crystal Plasticity*, Elsevier, 2003.
- [30] F. Dalla Torre, P. Spätig, R. Schäublin, M. Victoria, Deformation behaviour and microstructure of nanocrystalline electrodeposited and high pressure torsioned nickel, *Acta Mater* 53 (2005) 2337–2349.
- [31] Z.H. Cao, L. Wang, K. Hu, Y.L. Huang, X.K. Meng, Microstructural evolution and its influence on creep and stress relaxation in nanocrystalline Ni, *Acta Mater* 60 (2012) 6742–6754.
- [32] L. Lu, T. Zhu, Y. Shen, M. Dao, K. Lu, S. Suresh, Stress relaxation and the structure size-dependence of plastic deformation in nanotwinned copper, *Acta Mater* 57 (2009) 5165–5173.
- [33] G. Wang, Z. Jiang, H. Zhang, J. Lian, Enhanced tensile ductility in an electrodeposited nanocrystalline copper, *J. Mater. Res.* 23 (2008) 2238–2244.
- [34] G. Wang, Z. Jiang, Q. Jiang, J. Lian, Mechanical behavior of an electrodeposited nanostructured Cu with a mixture of nanocrystalline grains and nanoscale growth twins in submicrometer grains, *J. Appl. Phys.* 104 (2008) 084305.
- [35] S. Plimpton, Fast parallel algorithms for short-range molecular dynamics, *J. Comput. Phys.* 117 (1995) 1–19.
- [36] Y. Mishin, M.J. Mehl, D.A. Papaconstantopoulos, A.F. Voter, J.D. Kress, Structural stability and lattice defects in copper: *Ab initio*, tight-binding, and embedded-atom calculations, *Phys. Rev. B* 63 (2001) 224106.
- [37] S. Nosé, A molecular dynamics method for simulations in the canonical ensemble, *Mol. Phys.* 52 (1984) 255–268.
- [38] W.G. Hoover, Canonical dynamics: equilibrium phase-space distributions, *Phys. Rev. A* 31 (1985) 1695–1697.
- [39] M. Parrinello, A. Rahman, Polymorphic transitions in single crystals: a new molecular dynamics method, *J. Appl. Phys.* 52 (1981) 7182–7190.
- [40] A. Stukowski, Visualization and analysis of atomistic simulation data with OVITO—the open visualization tool, *Model. Simul. Mater. Sci. Eng.* 18 (2010) 015012.
- [41] G.E. Dieter, D. Bacon, *Mechanical Metallurgy*, McGraw-Hill, New York, 1986.
- [42] C.Y. Jeong, S.W. Nam, J. Ginszler, Activation processes of stress relaxation during hold time in 1Cr-Mo-V steel, *Mater. Sci. Eng. A* 264 (1999) 188–193.
- [43] B.L. Mordike, P. Haasen, The influence of temperature and strain rate on the flow stress of  $\alpha$ -iron single crystals, *Philos. Mag.* 7 (1962) 459–474.
- [44] H. Conrad, On the Mechanism of Yielding and Flow in Iron, *Atomics International. Div. of North American Aviation, Inc., Canoga Park, Calif.*, 1961.
- [45] A.K. Mukherjee, J.E. Bird, J.E. Dorn, Experimental correlations for high-temperature creep, *Trans. A.S.M.* 62 (1969) 155–179.
- [46] J. Hutchinson, K. Neale, Influence of strain-rate sensitivity on necking under uniaxial tension, *Acta Metall.* 25 (1977) 839–846.
- [47] H. Conrad, Grain-size dependence of the flow stress of Cu from millimeters to nanometers, *Metall. Mater. Trans. A* 35 A (2004) 2681–2695.
- [48] M.A. Meyers, A. Mishra, D.J. Benson, Mechanical properties of nanocrystalline materials, *Prog. Mater. Sci.* 51 (2006) 427–556.
- [49] H. Van Swygenhoven, A. Caro, Plastic behavior of nanophase metals studied by molecular dynamics, *Phys. Rev. B* 58 (1998) 11246–11251.
- [50] W. Dickenschied, R. Birringer, H. Gleiter, O. Kanert, B. Michel, B. Günther, Investigation of self-diffusion in nanocrystalline copper by NMR, *Solid State Commun.* 79 (1991) 683–686.
- [51] B. Cai, Q.P. Kong, L. Lu, K. Lu, Low temperature creep of nanocrystalline pure copper, *Mater. Sci. Eng. A* 286 (2000) 188–192.
- [52] J. Horváth, R. Birringer, H. Gleiter, Diffusion in nanocrystalline material, *Solid State Commun.* 62 (1987) 319–322.
- [53] Y.M. Wang, A.V. Hamza, E. Ma, Activation volume and density of mobile dislocations in plastically deforming nanocrystalline Ni, *Appl. Phys. Lett.* 86 (2005) 1–3.
- [54] C.C. Koch, Optimization of strength and ductility in nanocrystalline and ultrafine grained metals, *Scr. Mater* 49 (2003) 657–662.
- [55] S. Mahajan, D.E. Barry, B.L. Eyre, A thin twin and its interaction with a coherent twin boundary in copper, *Philos. Mag.* 21 (1970) 43–52.
- [56] J.W. Christian, S. Mahajan, Deformation twinning, *Prog. Mater. Sci.* 39 (1995) 1–157.
- [57] L. Lu, R. Schwaiger, Z.W. Shan, M. Dao, K. Lu, S. Suresh, Nano-sized twins induce high rate sensitivity of flow stress in pure copper, *Acta Mater* 53 (2005) 2169–2179.